

Time-resolved observations of water oxidation intermediates on a cobalt oxide nanoparticle catalyst

Miao Zhang, Moreno de Respinis[†] and Heinz Frei^{*}

In any artificial photosynthetic system, the oxidation of water to molecular oxygen provides the electrons needed for the reduction of protons or carbon dioxide to a fuel. Understanding how this four-electron reaction works in detail is important for the development of improved robust catalysts made of Earth-abundant materials, like first-row transition-metal oxides. Here, using time-resolved Fourier-transform infrared spectroscopy and under reaction conditions, we identify intermediates of water oxidation catalysed by an abundant metal-oxide catalyst, cobalt oxide (Co₃O₄). One intermediate is a surface superoxide (three-electron oxidation intermediate absorbing at 1,013 cm⁻¹), whereas a second observed intermediate is attributed to an oxo Co(IV) site (one-electron oxidation intermediate absorbing at 840 cm⁻¹). The temporal behaviour of the intermediates reveals that they belong to different catalytic sites. Knowledge of the structure and kinetics of surface intermediates will enable the design of improved metal-oxide materials for more efficient water oxidation catalysis.

Oxidation of water to molecular oxygen is a step common to all approaches to converting sunlight to fuel, whether biological or artificial^{1,2}. The reason for this is that the end products of spent solar fuel or biofuel, either in a combustion process or at the exhaust of a fuel cell, are carbon dioxide and water. Therefore, in order for renewable fuel generation and utilization to be cyclic, without accumulation of by-products, water molecules need to serve as the electron source for the photosynthetic process. As a consequence, understanding Nature's water oxidation mechanism in photosystem II (from green plants and bacteria) has been the focus of research for several decades³. Although the structure of the Mn₄O₄Ca complex has recently been established by single-crystal X-ray diffraction with high resolution⁴, the precise nature of critical mechanistic steps such as OO bond formation and oxygen release remain the subject of debate.

In the case of artificial photosystems, catalysts for water oxidation in the form of clusters, nanoparticles or thin films of first-row transition-metal oxides have attracted particular attention in recent years. Important features include the Earth abundance of these materials (which is a critical factor because of the need to make solar fuel generators on a very large scale), the robustness of solid oxides, and opportunities for catalytic efficiency improvement by increasing the surface area through nanostructuring. Solid oxide anodes of mainly first row transition metals are already utilized in commercial alkaline electrolyzers^{5,6}. Recent substantive progress in enhancing catalytic rates at moderate overpotential opens up their use in artificial photosystems. This includes new methods for preparing electrodeposited films of cobalt oxide^{7,8} or nickel oxide⁹ on anodes, and nanostructured Co₃O₄ or manganese oxide clusters embedded in mesoporous silica scaffolds^{10,11} or on silica nanoparticle surfaces¹². The latter are driven by a visible light sensitizer. Highly electrocatalytically active monodisperse Co₃O₄ nanoparticles¹³ and thin films of manganese oxide^{14,15} have been reported, and promising materials now include multi-metal nanoparticle catalysts such as CaMn₂O₄ (ref. 16), Li₂Co₂O₄ (ref. 17) and NiFe₂O₄ (ref. 18). Furthermore, molecularly defined metal oxides in the form of polyoxo-metallates,

featuring a core made of abundant elements such as cobalt, have been established as efficient water oxidation catalysts¹⁹.

For Earth-abundant metal-oxide catalysts, some mechanistic aspects of the four-electron cycle of water oxidation were recently inferred from combined electrokinetic/cyclic voltammetric studies, specifically a fast pre-equilibrium preceding the OO bond-forming reaction in the case of cobalt oxide films electrodeposited from phosphate or other salt solutions and a choice of buffer^{20,21}. *Ex situ* electron paramagnetic resonance (EPR) analysis of electrocatalytic cobalt oxide films following electrochemical runs indicated the build-up of Co(IV)=O species^{21,22}, and cobalt X-ray absorption near-K-edge structure spectroscopy during water oxidation catalysis confirmed a cobalt valence greater than III²³. Optical absorption signals were reported in a couple of electrocatalytic systems: a band at 510 nm upon onset of electrocatalysis at δ-MnO₂ films, attributed to Mn³⁺ (ref. 24), and a transient absorption signal at 650 nm for a haematite (Fe₂O₃) photoanode, assigned to long-lived photoholes driving water oxidation^{25–29}. The bands indicate the formation of catalytic intermediates, but their chemical nature could not be specified. Ultraviolet light-induced water splitting at TiO₂ (rutile) films monitored by steady-state Fourier transform infrared (FTIR) spectroscopy revealed the build-up of surface peroxide moieties³⁰. Nonetheless, in the absence of temporal resolution, the kinetic relevancy or position of these species in the photocatalytic cycle could not be addressed. Yet, knowledge of individual events in the four-electron cycle of water oxidation on the catalyst surface through observation of structurally identified species and their temporal behaviour is required to uncover kinetic bottlenecks and to provide insights regarding design changes to overcome them.

Here, we report the first direct, temporally resolved observation of surface intermediates of water oxidation at a first-row metal-oxide catalyst, namely Co₃O₄ in the form of single crystal nanoparticles. The method used is rapid-scan FTIR spectroscopy in the attenuated total reflection (ATR) mode of visible light-sensitized catalysis in aqueous solution, which provides compelling evidence for the kinetic relevancy of the observed intermediates.

Physical Biosciences Division, Lawrence Berkeley National Laboratory, University of California, Berkeley, California 94720, [†]Present address: Delft University of Technology, Department of Chemical Engineering, PO Box 5045, 2600GA Delft, The Netherlands. *e-mail: hmfrei@lbl.gov

Results and discussion

A convenient method of driving the Co_3O_4 water oxidation catalyst is by hole injection from a visible light sensitizer, $[\text{Ru}(\text{bpy})_3]^{2+}$ ($\text{bpy} = 2,2'$ -bipyridine), in the presence of an $\text{S}_2\text{O}_8^{2-}$ electron acceptor. The $[\text{Ru}(\text{bpy})_3]^{3+}$ species, which is generated by absorption of a 476 nm light pulse followed by electron transfer to the persulfate acceptor, sequentially transfers holes to Co_3O_4 upon collision with the catalyst particles in aqueous suspension¹⁰ (for a detailed explanation of the process see Supplementary Scheme 1 and Supplementary Fig. 1). Two transient infrared bands attributed to different surface reaction intermediates were observed in the rapid-scan FTIR spectra in aqueous solution at pH 8. In H_2O , one absorption band appears at $1,013\text{ cm}^{-1}$ (species $\text{B}_{1013\text{ cm}^{-1}}$) and another at 840 cm^{-1} (species $\text{A}_{840\text{ cm}^{-1}}$), each with distinctly different kinetic behaviour.

Spectroscopy and kinetics of fast catalytic site. The $\text{B}_{1013\text{ cm}^{-1}}$ species has isotopic counterparts at 995 and 966 cm^{-1} in H_2^{18}O , and at 975 cm^{-1} in D_2O . Traces recorded at 5.85 s after the start of the 300 ms photolysis pulse for each of these isotopic experiments are presented in Fig. 1 (traces a–c) (complete survey FTIR difference spectra are presented in Supplementary Fig. 3). To rule out the possibility of spectral interference of the sensitizer and the reaction intermediate, experiments were repeated under identical conditions with perdeuterated $[\text{Ru}(\text{bpy-d}_8)_3]^{2+}$

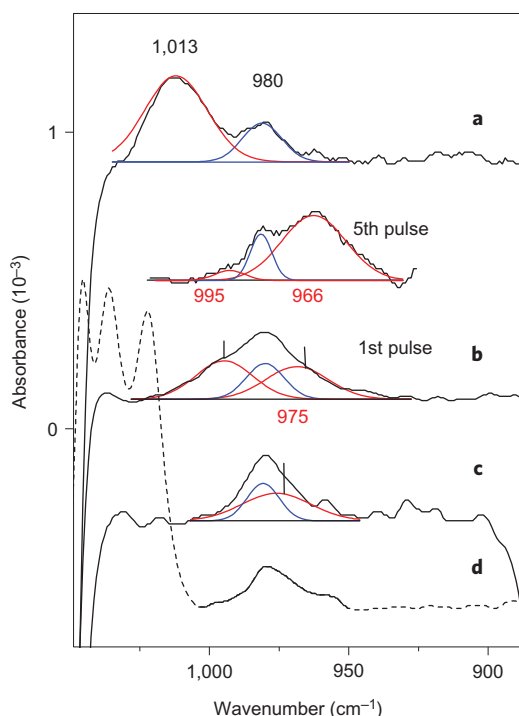


Figure 1 | Rapid-scan FTIR spectra of water oxidation catalysis. Bands assigned to superoxide intermediate $\text{Co}(\text{III})-(\text{OO})\text{Co}(\text{III})$ in parent and isotopic water solution at 5,850 ms after onset of the 300 ms photolysis laser pulse (476 nm, 160 mW). The sensitizer was $[\text{Ru}(\text{bpy-h}_8)_3]^{2+}$. Traces **a–d**: H_2^{16}O (**a**); H_2^{18}O (**b**); D_2O (**c**); control experiment in H_2^{16}O , no Co_3O_4 present (**d**). The dotted signal in this trace is due to unreacted $[\text{Ru}(\text{bpy-h}_8)_3]^{3+}$. Red components: superoxide bands; blue component: SO_4^{2-} growth. The deconvolution procedure is described in the Supplementary Information page 11. The inset of **b** shows the spectral trace after irradiation with five laser pulses, each of 300 ms duration. The intensity gain of the 966 cm^{-1} band ($^{18}\text{O}^{18}\text{O}$ stretch mode) relative to 995 cm^{-1} ($^{16}\text{O}^{18}\text{O}$ mode) between the first and fifth light pulse driving the water oxidation catalysis directly manifests the incorporation of ^{18}O from H_2^{18}O molecules into the coordination sphere of surface cobalt centres.

sensitizer, leading to results identical to those shown in Supplementary Fig. 2. The band at 980 cm^{-1} originates from SO_4^{2-} , the reduced acceptor, as confirmed by the correct intensity ratio with respect to the $1,104\text{ cm}^{-1}$ absorption of sulfate anion.

The appearance of two bands with ^{18}O isotopic shifts of 18 and 47 cm^{-1} indicates OO bond stretch modes of $^{18}\text{O}^{16}\text{O}$ and $^{18}\text{O}^{18}\text{O}$ moieties. For OO stretch modes of partially labelled superoxide and peroxide moieties, the reported isotope shifts are $20\text{--}30\text{ cm}^{-1}$ (refs 31,32) and, for fully labelled OO bonds, between 44 and 61 cm^{-1} (refs 31,33). The infrared frequency of $\text{B}_{1013\text{ cm}^{-1}}$ is lower than expected for free superoxide species (O_2^-), which typically absorb in the range $1,200\text{--}1,070\text{ cm}^{-1}$ (ref. 31). On the other hand, the band position is too high for peroxide moieties (CoOOH or CoOOCo); OO stretching modes of peroxides lie in the $920\text{--}740\text{ cm}^{-1}$ region³¹. However, it agrees well with a superoxide moiety on a metal-oxide surface as reported for CoO-MgO solid solution, where OO^- forms a μ -superoxo bridge between two metal centres³⁴. Furthermore, inorganic molecular analogues of bridged superoxo complexes of $\text{Co}(\text{III})$ centres such as μ -superoxo- μ -amido-bis[tetra-amminecobalt(III)] were reported and possess an OO mode at $1,068\text{ cm}^{-1}$ (refs 35,36). Hydrogen-bonding interaction (see below) would cause a several tens of cm^{-1} redshift, with an OO band anticipated around $1,000\text{ cm}^{-1}$. Although comparison with model systems featuring organic ligands is less straightforward, systems with superoxo modes around $1,000\text{ cm}^{-1}$ have been reported^{37,38}. The modest but distinct D isotope shift of 38 cm^{-1} to lower frequencies implies that a hydrogen is interacting with the intermediate. Spectral evidence for hydrogen bonding of a superoxo moiety with neighbouring OH groups on a cobalt oxide surface has been reported in the literature³⁹. Therefore, $\text{B}_{1013\text{ cm}^{-1}}$ is proposed to possess a $\text{Co}(\text{III})\text{OO}$ group with superoxide electronic structure that is hydrogen-bonded to an adjacent CoOH (CoOD) or possibly another hydroxyl group such as a protonated bridging oxygen. We conclude that a superoxide surface intermediate has been detected, which constitutes the three-electron water oxidation species just one oxidation step short of O_2 elimination.

Mass spectroscopy was used to monitor oxygen gas accumulated in the head space of the H_2^{18}O solution following photolysis on the timescale of tens of minutes. Gas aliquots released periodically into the mass spectrometer showed m/z 36 as the predominant product (with a ratio of 8:1 for m/z 36: m/z 34), whereas m/z 32 was not detected at all (Supplementary Fig. 4; note that the absence of $^{16}\text{O}_2$ product or unlabelled superoxide intermediate in the H_2^{18}O experiment rules out any role by unspecified side oxide species in side reactions unrelated to water oxidation). According to Fig. 1b, FTIR spectra after a single 300 ms light pulse show approximately equal intensity for the 995 cm^{-1} ($^{18}\text{O}^{16}\text{O}$) and 966 cm^{-1} ($^{18}\text{O}^{18}\text{O}$) superoxide intermediates. However, after just five consecutive light pulses (inset of Fig. 1b, total photolysis time of 1.5 s), the $^{18}\text{O}^{18}\text{O}/^{18}\text{O}^{16}\text{O}$ ratio of the superoxide absorption is 8:1 (within uncertainty). The agreement between the isotopic composition of the O_2 product and the three-electron oxidation intermediate on the Co_3O_4 surface demonstrates that the observed superoxide species is a kinetically competent intermediate of the photocatalytic oxygen evolving cycle. Furthermore, monitoring of O_2 build-up in solution with an electrochemical detection method (O_2 -selective Clark electrode) allowed quantitative measurement of the oxygen yield following illumination with a single 476 nm laser pulse of 300 ms duration. Interestingly, a significantly reduced O_2 yield was found compared to the build-up expected based on the O_2 yield observed with a longer laser pulse of 1 s duration. As shown in Fig. 2, the yield of O_2 following a 300 ms light pulse is only 20% of the build-up observed after a 1 s pulse, not 30%, as expected based on the number of photons. This means that, upon 300 ms illumination, one-third fewer water oxidation cycles are completed and release O_2 compared to illumination for 1 s. The result agrees well with

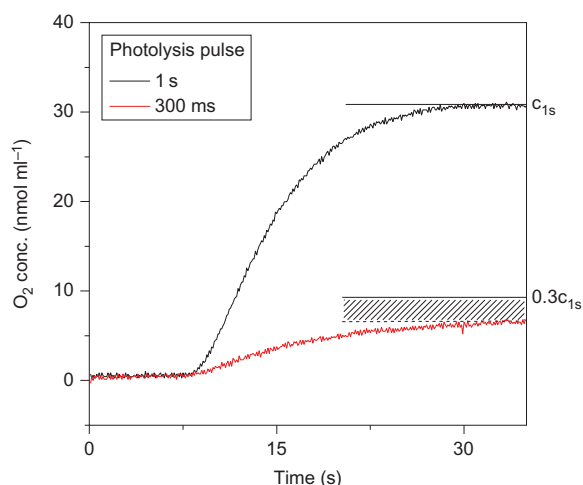


Figure 2 | Electrochemical monitoring of oxygen evolution by photolysis pulse. Black: sample irradiated with a 1 s duration pulse of 476 nm laser emission (160 mW). Red: sample irradiated with a 300 ms duration pulse. The shaded section indicates the missing O_2 in the 300 ms experiment, which is still present as intermediates on the Co_3O_4 surface. For the 1-s pulse experiment, the fraction of incomplete catalytic cycles is much smaller but not zero (Supplementary Fig. 6). c_{1s} indicates the observed oxygen concentration generated by a 1-s light pulse; $0.3c_{1s}$ indicates the expected oxygen concentration of a 300 ms light pulse based on the number of photons.

the observation that surface intermediates are still present in the form of superoxide species at the end of the short pulse. This outcome was reproduced in D_2O solution (Supplementary Fig. 5).

The kinetic behaviour of the superoxide surface intermediate, shown in Fig. 3, indicates that the species continues to be produced in a dark reaction after termination of the 300 ms light pulse. However, growth stops as soon as the residual $[Ru(bpy)_3]^{3+}$ has disappeared (shown in Fig. 3 by the kinetic trace of its $1,496\text{ cm}^{-1}$ band; Supplementary Table 1). This indicates that the surface superoxide is formed by continued hole injection from $[Ru(bpy)_3]^{3+}$ into Co_3O_4 particles. The $1,013\text{ cm}^{-1}$ band (and its D and ^{18}O counterparts at 995 and 966 cm^{-1} ; Supplementary Fig. 7) decreases very slowly on the timescale of seconds once $[Ru(bpy)_3]^{3+}$ is consumed, and even then by no more than one-third of the peak absorbance after 6 s. We attribute this slow diminishment to diffusion of Co_3O_4 nanoparticles and reaction of the surface superoxide sites upon collision with other Co_3O_4 particles, rather than a spontaneous dark reaction on the isolated catalyst particles. The result strongly suggests that reaction of the superoxide surface intermediate requires hole injection through continued illumination, resulting in oxidation under elimination of O_2 .

Spectroscopy and kinetics of slow catalytic site. A second band in the rapid-scan FTIR experiment was observed at 840 cm^{-1} (Fig. 4a, sensitizer $[Ru(bpy-h_8)_3]^{2+}$; Supplementary Fig. 8, sensitizer $[Ru(bpy-d_8)_3]^{2+}$), with a decay time of $0.99 \pm 0.05\text{ s}$ (293 K), as shown in Fig. 5. No significant ^{18}O or D isotope frequency shifts were observed when using $H_2^{18}O$ or D_2O (Fig. 4b,c). The decay kinetics was the same in all isotopic aqueous solutions (Fig. 5, Supplementary Fig. 9).

The very different kinetic behaviour of the $1,013\text{ cm}^{-1}$ and 840 cm^{-1} bands indicates that they originate from different surface species. The 840 cm^{-1} absorption is in the frequency range typical for a peroxide OO stretch mode³¹. However, because only (partially or fully) ^{18}O labelled oxygen gas ($m/z\ 34$ and $m/z\ 36$) was detected in the photocatalytic experiment in $H_2^{18}O$, the absence of an isotopic frequency shift of $A_{840\text{ cm}^{-1}}$ rules out assignment to a peroxide intermediate. The band must therefore be a

Co–O stretching mode with the oxygen originating from the (unlabelled) Co_3O_4 surface. Symmetric and asymmetric stretch modes of Co_3O_4 absorb in the spectral range below 690 cm^{-1} (ref. 40), which leaves, as a remaining possibility, assignment to a Co–O mode with the cobalt in a higher oxidation state. From a mechanistic standpoint, a Co(IV) centre is most probable. Although we are not aware of reports of Co(IV)=O vibrational modes in the literature, surface Co(IV) oxide moieties have been detected by *ex situ* EPR spectroscopy in electrodeposited cobalt oxide films^{21,22}, and have been reported for coordination compounds^{41–44}. The Co(IV)=O mode is expected in the same region as the Fe(IV)=O mode, which lies between 834 and 818 cm^{-1} (ref. 45). We propose assignment of the 840 cm^{-1} band to a surface Co(IV)=O site, formed by oxidation of a surface Co(III)–OH group upon transfer of a hole from $[Ru(bpy)_3]^{3+}$ to Co_3O_4 under concurrent loss of a proton. This step most likely constitutes the first hole transfer from $[Ru(bpy)_3]^{3+}$ to Co_3O_4 that initiates the four-electron oxidation cycle.

The fact that the final O_2 product is already detected after a single 300 ms visible light pulse in the electrochemical experiment while $A_{840\text{ cm}^{-1}}$ decays with a time constant of 1 s means that this surface intermediate does not contribute to the observed O_2 evolution for a light pulse duration of just 300 ms. The lack of photocatalytic turnover of this site during a 300 ms pulse is further confirmed by the absence of Co(IV)= ^{18}O formation in the $H_2^{18}O$ experiment. Moreover, the rise of the superoxide species $B_{1013\text{ cm}^{-1}}$ is much faster than the decay of $A_{840\text{ cm}^{-1}}$, which means that $A_{840\text{ cm}^{-1}}$ is not a precursor of $B_{1013\text{ cm}^{-1}}$. We conclude that $A_{840\text{ cm}^{-1}}$ is a catalytic site on the Co_3O_4 particle surface with substantially slower water oxidation kinetics.

Proposed catalytic mechanism. A common feature of cyclic voltammetry analyses of Co_3O_4 water oxidation catalysts and electrodeposited cobalt oxide films is how well they agree with Pourbaix analyses of layered double hydroxide structures, the key motifs of which are Co(OH)–O–CoOH sites of adjacent CoOH groups²¹. Adjacent oxo-bridged Co(III) centres in octahedral coordination are present on the various crystallographic surfaces of Co_3O_4 , including the energetically preferred (001) surface,

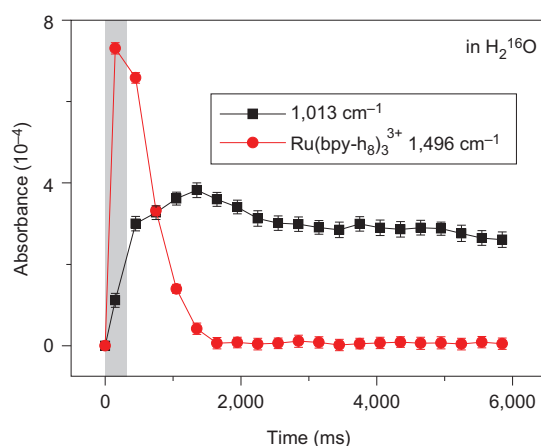


Figure 3 | Temporal behaviour of superoxide surface intermediate. The infrared bands of superoxide intermediate ($1,013\text{ cm}^{-1}$) and oxidized sensitizer $Ru(bpy-h_8)_3^{3+}$ ($1,496\text{ cm}^{-1}$) on visible light-sensitized water oxidation at Co_3O_4 catalyst in $H_2^{16}O$. The 300 ms laser pulse duration is indicated by the grey area. Error bars represent half the peak-to-peak height of the noise level. The lack of spontaneous reaction of $B_{1013\text{ cm}^{-1}}$ over a time span of 6 s indicates that expulsion of the O_2 and restart of the catalytic cycle requires the arrival of another hole induced by photoexcitation of the sensitizer.

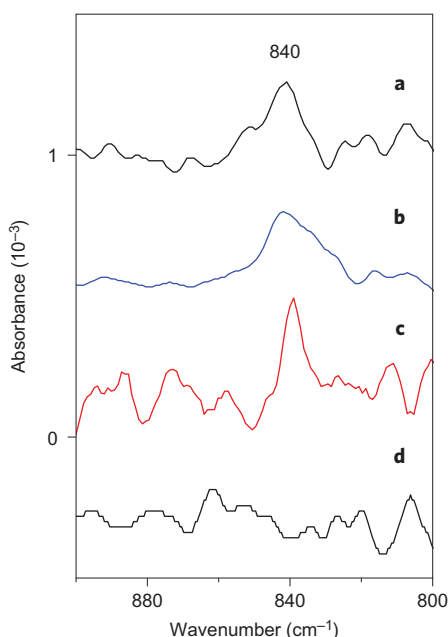


Figure 4 | Rapid-scan FTIR spectra of water oxidation catalysis. $A_{840\text{ cm}^{-1}}$ species with band assigned to Co(IV)=O in parent and isotopic water solution at 450 ms after onset of the 300 ms photolysis pulse (476 nm, 160 mW). The sensitizer was $[\text{Ru}(\text{bpy}-\text{h}_8)_3]^{2+}$. Traces **a-d**: H_2^{16}O (**a**); H_2^{18}O (**b**); D_2O (**c**); control experiment in H_2^{16}O , no Co_3O_4 present (**d**). The absence of an ^{18}O isotopic frequency shift implies that the O of $A_{840\text{ cm}^{-1}}$ originates from the (unlabelled) Co_3O_4 catalyst particle, and that no catalytic turnover occurs during a 300 ms photosensitization pulse.

which closely resembles the local environment of cobalt oxy hydroxide Co(O)OH^{46-48} . Hence, the Co(OH)-O-CoOH motif is readily realized on OH-terminated Co_3O_4 surfaces. It is interesting to note that, under electrocatalytic conditions, conversion of Co_3O_4 to the hydroxyl-rich Co(O)OH structure occurs at 0.75 V (pH 7) according to electrokinetic measurements⁴⁹ and *in situ* Raman spectroscopy⁵⁰. In the case of cobalt oxide films, the fast pre-equilibrium preceding the OO bond-forming reaction was assigned to the conversion of a resting-state $\text{Co(IV)(=O)-O-Co(III)-OH}$ to $\text{Co(IV)(=O)-O-Co(IV)=O}$ accompanied by proton transfer, which is supported by a computational study on a cubane model cluster^{20,21,51}. Accordingly, we propose for the fast catalytic cycle the four-electron water oxidation mechanism shown in Fig. 6a. Two sequential hole injections convert the adjacent Co(III)-OH groups to Co(IV)=O centres (the electronic structure might be more closely represented as a resonance between Co(IV)=O and Co(III)-O^{\cdot})⁵¹. Subsequent spontaneous (dark) nucleophilic addition of H_2O to one of the oxo sites results in OO bond formation and a hydroperoxide surface species, with both metal centres reduced to Co(III) . This step is analogous to the reactive $\text{Ru(V)(=O)-O-Ru(V)=O}$ state of the Ru blue dimer⁵². Owing to the complete absence of unlabelled superoxide intermediate $\text{B}_{1013\text{ cm}^{-1}}$ or final O_2 product in the H_2^{18}O experiment, direct coupling of two neighbouring Co(IV)=O groups to yield O_2 or a peroxide bridged intermediate⁴⁴, or O_2 elimination from the $\text{Co(IV)(=O)-O-Co(IV)=O}$ intermediate with one O originating from Co=O and the other from the O bridge between the two Co is ruled out. Subsequent oxidation by another injected hole produces the observed superoxide surface site. It is interesting to note that this latter oxidation step results in the oxidation of the peroxide OO moiety to superoxide, rather than an increase of the oxidation state of Co(III) to form a Co(IV) hydroperoxo species.

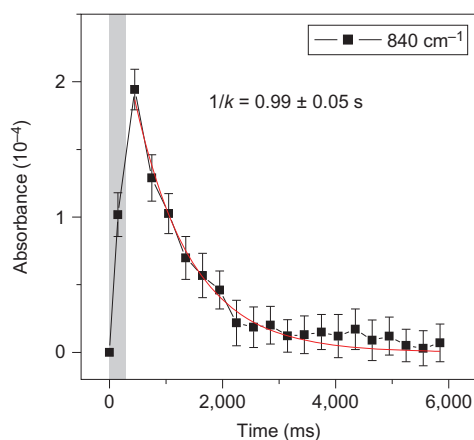


Figure 5 | Temporal behaviour of the 840 cm^{-1} intermediate assigned to Co(IV)=O . The decay following a 476 nm laser pulse is shown for Co_3O_4 catalyst in H_2^{16}O . The duration of the 300 ms laser pulse is indicated by the grey area. Sensitizer: $[\text{Ru}(\text{bpy}-\text{h}_8)_3]^{2+}$. Error bars represent half the peak-to-peak height of the noise level. As a consequence of the 1 s duration of the decay (attributed to OO bond formation with H_2O), the photocatalytic cycle of the $A_{840\text{ cm}^{-1}}$ species does not close when initiated by a 300 ms photosensitization pulse.

For a light pulse of 300 ms duration, the reaction at the majority of fast sites is advanced to the superoxo state and even liberation of O_2 . Build-up of Co(IV)=O and Co(III)OOH intermediates (Fig. 6a) at the fast site during the light pulse is too small for detection at the spectral sensitivity currently attainable in the $800\text{--}700\text{ cm}^{-1}$ region. In H_2^{18}O , oxidation of the rate-limiting superoxide intermediate under elimination of oxygen and regeneration of adjacent Co(III)-OH groups by coordination of water at the open Co(III) site leads to partially labelled ^{18}O superoxo in the next, and increasingly fully labelled intermediates and O_2 product in the subsequent cycles. The observation of some fully labelled superoxide even after a single 300 ms pulse indicates that a substantial fraction of the fast catalytic sites cycle multiple times during the photolysis pulse, indicating a turnover frequency (TOF) $> 3\text{O}_2\text{ s}^{-1}$ per fast catalytic surface site. This is two orders of magnitude larger than the lower limit of $\text{TOF} \geq 0.02\text{O}_2\text{ s}^{-1}$ per cobalt surface site (at pH 8) estimated for a 5 nm Co_3O_4 particle if one assumes that all surface cobalt centres are active. Note that O exchange of Co_3O_4 with water molecules occurs exclusively through the water oxidation cycle; no exchange of the ^{18}O of H_2^{18}O into unlabelled Co_3O_4 was detected when suspending Co_3O_4 particles in H_2^{18}O under visible light illumination (in the absence of sensitizer) for 8 h (Supplementary Fig. 10).

We propose that the structural difference between the fast catalytic site and the slowly reacting Co(IV)=O site at 840 cm^{-1} is the absence of an adjacent Co(III)OH group in the case of $A_{840\text{ cm}^{-1}}$. As a result, there is no adjacent Co(IV)=O group formed during the catalytic cycle at the slow site, depriving the isolated Co(IV)=O group of the additional oxidizing power of an electronically coupled second Co(IV) centre. Furthermore, the lack of a neighbouring Co(IV)=O group requires deprotonation of the H_2O molecule upon addition to the Co(IV)=O site, in contrast to OO bond formation at the fast catalytic site. As a result, the proposed spontaneous OO bond-forming reaction to yield Co(II)OOH ($1/e$ time of 0.99 s^{-1}) is at least ten times slower (and probably much more so) than the OO bond-forming step at the fast catalytic site (Fig. 6b). With a reaction time well beyond the duration of the photolysis pulse, the slow site does not advance beyond the hydroperoxide state following a single 300 ms pulse. The OO band of Co(II)OOH is not observed, most likely because it absorbs below 750 cm^{-1} , a region rendered opaque by solvent absorption (H_2O tumbling motion)⁵³. The OO

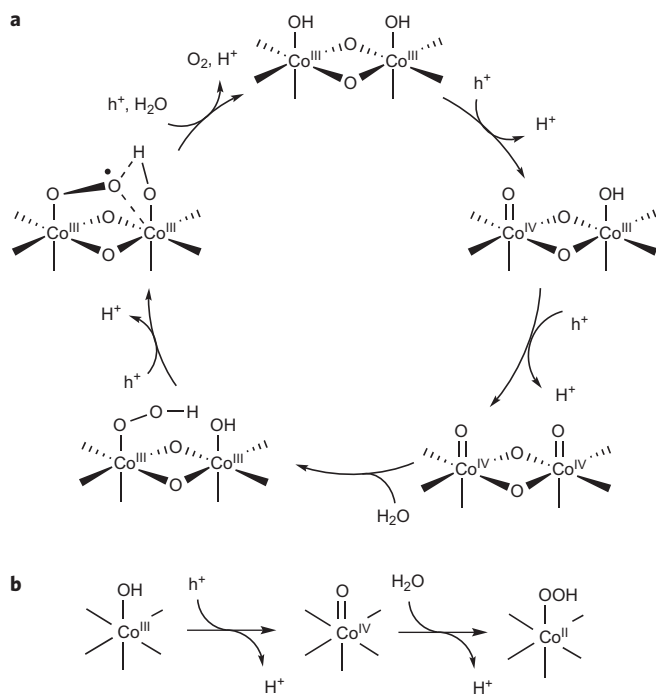


Figure 6 | Proposed photocatalytic mechanism. a, Water oxidation mechanism of the fast Co₃O₄ surface site. **b**, Mechanism of the slow Co₃O₄ surface site. The OO bond-forming step with H₂O in the fast cycle features the cooperative effect of adjacent electronically coupled Co(IV)=O sites, which is absent in the H₂O addition reaction at the slow site.

stretch modes of transition-metal centres in a low valence state such as Co(II) are strongly redshifted⁵⁴ relative to peroxide modes of high valent groups like Co(III)OOH (828 cm⁻¹)³, Ti(IV)OOH (838 cm⁻¹) or Ir(V)OOH (830 cm⁻¹) (refs 33,30,53, respectively).

Conclusions

Two surface intermediates of visible light-sensitized water oxidation at an abundant metal-oxide catalyst, Co₃O₄, were detected by rapid-scan FTIR spectroscopy. The agreement of the ¹⁸O isotopic composition of a surface superoxide species and the final O₂ gas product provides compelling evidence for the kinetic competency of this three-electron oxidation intermediate. At a fast catalytic site, the superoxide intermediate grows and O₂ evolves within a 300 ms photolysis pulse (TOF > 3 s⁻¹). By contrast, a slow site marked by a Co(IV)=O group does not advance beyond the one-electron intermediate within the same 300 ms pulse. The widely different photocatalytic efficiency of the two types of site is attributed to the presence/absence of adjacent Co(III)OH groups coupled via an oxygen bridge. Improvement of the sensitivity of the ATR method should allow time-resolved FTIR monitoring with shorter photolysis pulses, which, in turn, will enable detection and kinetic analysis of the early (one- and two-electron) surface intermediates of the fast site.

Having established, in this work, the first structurally identified intermediates of an abundant metal-oxide catalyst for water oxidation under reaction conditions, we can now address the question of how charge flow from a light absorber (whether a molecule or a semiconductor photoanode) drives sequential chemical transformations on the catalyst surface^{26,28,55}. Knowledge of the structure and kinetics of surface intermediates opens up opportunities for tailoring the light absorber properties to the energetic requirements of each step in the photocatalytic cycle, and will enable design improvements towards more efficient photo-driven water oxidation catalysts.

Methods

Synthesis of Co₃O₄ nanocrystals. Single-crystal Co₃O₄ nanoparticles with an average size of 4 nm were synthesized with a surfactant-assisted solvothermal method, as reported previously⁵⁶. The prepared nanoparticles were dispersed in ethanol and stored at room temperature. For photocatalysis experiments, ethanol was removed and the nanoparticles dried before dispersal in water.

Time-resolved rapid-scan FTIR. An ATR accessory featuring a 3-mm-diameter diamond plate with three reflections (ASI Systems model PN 071-1213) was used for the time-resolved FTIR experiments. A drop of aqueous suspension containing Co₃O₄ colloid particles (0.4 μM), [Ru(bpy)₃]Cl₂ (Alfa-Aesar, 1 mM) and Na₂S₂O₈ (Sigma-Aldrich, 100 mM) in pH 8.5 buffer (NaHCO₃, Sigma-Aldrich, 0.5 M) was held on top of the diamond plate in a homemade Teflon liquid cell⁵³. For isotopic labelling experiments, H₂¹⁸O (ICON, 97.6% ¹⁸O) or D₂O (Cambridge Isotopes Laboratories, 99.9% D) was used. A 476 nm visible laser pulse of 300 ms duration (160 mW, area = 7 mm²) was generated by intercepting the continuous emission of an argon ion laser (Coherent model Innova 90 C) with a mechanical shutter (UniBlitz model D122). The photolysis laser pulse was steered towards the liquid suspension over the ATR plate for excitation of the [Ru(bpy)₃]²⁺ sensitizer.

Time-resolved rapid-scan FTIR spectra were recorded on a Bruker model Vertex 80 spectrometer equipped with a HgCdTe PV detector (Kolmar Technologies model KMPV11-1-J2, 14 μm bandgap). The mirror velocity was 160 kHz and the spectral resolution was 4 cm⁻¹. Data were recorded in double-sided/forward-backward mode. Opening of the mechanical shutter was triggered by the forward motion of the interferometer mirror for precise timing of reaction initiation and start of FTIR data acquisition (*t* = 0 of experiment)⁵³. For each sample, 1,000 spectra were recorded in the dark before photolysis and averaged. The resulting spectrum served as background. The protocol for obtaining the transient spectra consisted of the recording of 20 interferograms following the arrival of the laser pulse. Consequently, 20 spectral time slices at 300 ms time resolution were extracted, resulting in final absorbance spectra with midpoints at 150 ms, 450 ms, 750 ms, 1,050 ms and so on, up to 5,850 ms. The sample was discarded after each pulse. The results of 100 experiments were averaged for further signal-to-noise improvement.

Synthesis of [Ru(2,2'-dipyridyl-d₈)₃]Cl₂·xH₂O. The deuterated [Ru(2,2'-dipyridyl-d₈)₃]Cl₂·xH₂O was synthesized according to the literature⁵⁷. The FTIR bands of the isotopomer in reduced and oxidized form are presented in Supplementary Table 1.

Water oxidation experiments. Oxygen evolution upon photochemical water oxidation in the aqueous phase was monitored by a Clark electrode equipped with a platinum cathode and an Ag/AgCl anode (Hansatech, Oxygraph system). The electrode was assembled by adding a drop of 0.1 M KCl electrolyte on the tip of the platinum electrode, then tightly covering it with a thin polytetrafluoroethylene (PTFE) membrane that was permeable to oxygen. Liquid-phase two-point calibration was performed by recording the current for an air-saturated solution and a deoxygenated solution at 295 K. In a typical photochemical water oxidation experiment, 1 ml of the solution was irradiated with 476 nm laser emission (160 mW), with the beam expanded to a diameter of 1 cm. Before irradiation, the solution was purged with N₂.

Mass spectrometry was used to monitor O₂ gas evolution in the head space of the solution. A volume of 2 ml of aqueous buffer (pH ~7.4, Na₂SiF₆-NaHCO₃, 0.02–0.04 M) containing Ru(bpy)₃Cl₂ (1 mM) and Na₂S₂O₈ (100 mM) was transferred to a 10 ml glass flask that served as reactor. The solution was purged with argon (ultrahigh purity, 99.999%, PraxAir) for 15 min. The catalyst was degassed in vacuum overnight and transferred to the reactor under an argon atmosphere, followed by argon purging of the mixture for another 15 min. The reactor was filled with 150 torr argon before start of photolysis. The reactor was irradiated with a 476 nm argon ion laser beam (30 mW) expanded to 1 cm diameter. A 2.5 ml aliquote of gas was periodically captured from the headspace of the reactor and injected into a quadrupole mass spectrometer (Pfeiffer model Omnistar 422). The reactor was kept in the dark for 30 min before irradiation in order to test for leaks, but no oxygen was observed.

Received 16 November 2013; accepted 14 January 2014;
published online 23 February 2014

References

- Lewis, N. S. & Nocera, D. G. Powering the planet: chemical challenges in solar energy utilization. *Proc. Natl Acad. Sci. USA* **103**, 15729–15735 (2006).
- Alstrum-Acevedo, J. H., Brennaman, M. K. & Meyer, T. J. Chemical approaches to artificial photosynthesis. 2. *Inorg. Chem.* **44**, 6802–6827 (2005).
- Pushkar, Y. *et al.* Structural changes in the Mn₄Ca cluster and the mechanism of photosynthetic water splitting. *Proc. Natl Acad. Sci. USA* **105**, 1879–1884 (2008).
- Umena, Y., Kawakami, K., Shen, J.-R. & Kamiya, N. Crystal structure of oxygen-evolving photosystem II at a resolution of 1.9 Å. *Nature* **473**, 55–60 (2011).
- Tilak, B. V. *et al.* in *Comprehensive Treatise of Electrochemistry* Vol. 2 (eds Bockris, J. O. M. *et al.*) 1–97 (Plenum, 1981).
- Trasatti, S. in *Electrochemistry of Novel Materials* (eds Lipkowsky, J. & Ross, P. N.) Ch. 5 (VCH Publishers, 1994).

7. Kanan, M. W. & Nocera, D. G. *In situ* formation of an oxygen-evolving catalyst in neutral water containing phosphate and Co^{2+} . *Science* **321**, 1072–1075 (2008).
8. Surendranath, Y., Dinca, M. & Nocera, D. G. Electrolyte dependent electrocatalysis and activity of cobalt based water oxidation catalysts. *J. Am. Chem. Soc.* **131**, 2615–2620 (2009).
9. Dinca, M., Surendranath, Y. & Nocera, D. G. Nickel-borate oxygen-evolving catalyst that functions under benign conditions. *Proc. Natl Acad. Sci. USA* **107**, 10337–10341 (2010).
10. Jiao, F. & Frei, H. Nanostructured cobalt oxide clusters in mesoporous silica as efficient oxygen-evolving catalysts. *Angew. Chem. Int. Ed.* **48**, 1841–1844 (2009).
11. Jiao, F. & Frei, H. Nanostructured manganese oxide clusters supported on mesoporous silica as efficient oxygen-evolving catalysts. *Chem. Commun.* **46**, 2920–2922 (2010).
12. Zidki, T. *et al.* Water oxidation catalyzed by cobalt(II) adsorbed on silica nanoparticles. *J. Am. Chem. Soc.* **134**, 14275–14278 (2012).
13. Esswein, A. J. *et al.* Size-dependent activity of Co_3O_4 nanoparticle anodes for alkaline water electrolysis. *J. Phys. Chem. C* **113**, 15068–15072 (2009).
14. Zaharieva, I. *et al.* Electrosynthesis, functional, and structural characterization of a water-oxidizing manganese oxide. *Energy Environ. Sci.* **5**, 7081–7089 (2012).
15. Gorlin, Y. & Jaramillo, T. F. A bifunctional nonprecious metal catalyst for oxygen reduction and water oxidation. *J. Am. Chem. Soc.* **132**, 13612–13614 (2010).
16. Najafpour, M. M. *et al.* Calcium manganese(III) oxides ($\text{CaMn}_2\text{O}_4 \cdot x\text{H}_2\text{O}$) as biomimetic oxygen-evolving catalysts. *Angew. Chem. Int. Ed.* **49**, 2233–2237 (2010).
17. Gardner, G. P. *et al.* Structural requirements in lithium cobalt oxides for the catalytic oxidation of water. *Angew. Chem. Int. Ed.* **51**, 1616–1619 (2012).
18. Hong, D. *et al.* Catalysis of nickel ferrite for photocatalytic water oxidation using $[\text{Ru}(\text{bpy})_3]^{2+}$ and $\text{S}_2\text{O}_8^{2-}$. *J. Am. Chem. Soc.* **134**, 19572–19575 (2012).
19. Yin, Q. *et al.* A fast soluble carbon-free molecular water oxidation catalyst based on abundant metals. *Science* **328**, 342–345 (2010).
20. Surendranath, Y., Kanan, M. W. & Nocera, D. G. Mechanistic studies of the oxygen evolution reaction by a cobalt-phosphate catalyst at neutral pH. *J. Am. Chem. Soc.* **132**, 16501–16509 (2010).
21. Gerken, J. B. *et al.* Electrochemical water oxidation with cobalt-based electrocatalysts from pH 0–14: the thermodynamic basis for catalyst structure, stability, and activity. *J. Am. Chem. Soc.* **133**, 14431–14442 (2011).
22. McAlpin, J. G. *et al.* EPR Evidence for Co(IV) species produced during water oxidation at neutral pH. *J. Am. Chem. Soc.* **132**, 6882–6883 (2010).
23. Kanan, M. W. *et al.* Structure and valency of a cobalt-phosphate water oxidation catalyst determined by *in situ* X-ray spectroscopy. *J. Am. Chem. Soc.* **132**, 13692–13701 (2010).
24. Takashima, T., Hashimoto, K. & Nakamura, R. Mechanism of pH-dependent activity for water oxidation to molecular oxygen by MnO_2 electrocatalysts. *J. Am. Chem. Soc.* **134**, 1519–1527 (2012).
25. Pendlebury, S. R. *et al.* Dynamics of photogenerated holes in nanocrystalline $\alpha\text{-Fe}_2\text{O}_3$ electrodes for water oxidation probed by transient absorption spectroscopy. *Chem. Commun.* **47**, 716–718 (2011).
26. Barroso, M. *et al.* Charge carrier trapping, recombination and transfer in hematite ($\alpha\text{-Fe}_2\text{O}_3$) water splitting photoanodes. *Chem. Sci.* **4**, 2724–2734 (2013).
27. Cummings, C. Y. *et al.* Kinetics and mechanism of light-driven oxygen evolution at thin film $\alpha\text{-Fe}_2\text{O}_3$ electrodes. *Chem. Commun.* **48**, 2027–2029 (2012).
28. Klahr, B. *et al.* Electrochemical and photoelectrochemical investigation of water oxidation with hematite electrodes. *Energy Environ. Sci.* **5**, 7626–7636 (2012).
29. Young, K. M. H. *et al.* Photocatalytic water oxidation with hematite electrodes. *Catal. Sci. Tech.* **3**, 1660–1671 (2013).
30. Nakamura, R. & Nakato, Y. Primary intermediates of oxygen photoevolution reaction on TiO_2 (rutile) particles revealed by *in situ* FTIR absorption and photoluminescence measurements. *J. Am. Chem. Soc.* **126**, 1290–1298 (2004).
31. Nakamoto, K. *Infrared and Raman Spectra of Inorganic and Coordination Compounds* 5th edn, 155 (Wiley, 1997).
32. Egan, J. W. *et al.* Crystal structure of a side-on superoxo complex of cobalt and hydrogen abstraction by a reactive terminal oxo ligand. *J. Am. Chem. Soc.* **112**, 2445–2446 (1990).
33. Rajani, C., Kincaid, J. R. & Petering, D. H. Resonance Raman studies of $\text{HOO-Co(III)bleomycin}$ and Co(III)bleomycin : identification of two important vibrational modes, $\nu(\text{Co-OOH})$ and $\nu(\text{O-OH})$. *J. Am. Chem. Soc.* **126**, 3829–3836 (2004).
34. Zecchina, A., Spoto, G. & Coluccia, S. Surface dioxygen adducts on MgO-CoO solid solutions: analogy with cobalt-based homogeneous oxygen carriers. *J. Mol. Catal.* **14**, 351–355 (1982).
35. Shibahara, T. & Mori, M. Raman and infrared spectra of $\mu\text{-O}_2$ dicobalt(III) complexes. *Bull. Chem. Soc. Jpn* **51**, 1374–1379 (1978).
36. Barraclough, C. G., Lawrance, G. A. & Lay, P. A. Characterization of binuclear $\mu\text{-peroxo}$ and $\mu\text{-superoxo}$ cobalt(III) amine complexes from Raman spectroscopy. *Inorg. Chem.* **17**, 3317–3322 (1978).
37. Urban, M. W., Nonaka, Y. & Nakamoto, K. Infrared and resonance Raman spectra of molecular oxygen adducts of $[\text{N,N}'\text{-ethylenebis(acetylacetonimino)}]_2$ cobalt(II). *Inorg. Chem.* **21**, 1046–1049 (1982).
38. Nour, E. M. & Hester, R. E. Resonance Raman studies of oxygen binding in cobalt(III)-salen complexes. *J. Mol. Struct.* **62**, 77–79 (1980).
39. Giamello, E., Sojka, Z., Che, M. & Zecchina, A. Spectroscopic study of superoxide species formed by low-temperature adsorption of oxygen onto cobalt oxide (CoO)–magnesium oxide solid solutions: an example of synthetic heterogeneous oxygen carriers. *J. Phys. Chem.* **90**, 6084–6091 (1986).
40. Shirai, H., Morioka, Y. & Nakagawa, I. Infrared and Raman spectra and lattice vibrations of some oxide spinels. *J. Phys. Soc. Jpn* **51**, 592–597 (1982).
41. Dimitrou, K. *et al.* Mixed-valence, tetranuclear cobalt(III,IV) complexes: preparation and properties of $[\text{Co}_4\text{O}_4(\text{O}_2\text{CR})_2(\text{bpy})_4]^{3+}$ salts. *Chem. Commun.* 1284–1285 (2001).
42. Pfaff, F. F. *et al.* An oxo cobalt(IV) complex stabilized by Lewis acid interactions with scandium(III) ions. *Angew. Chem. Int. Ed.* **50**, 1711–1715 (2011).
43. Lacy, D. C., Park, Y. J., Ziller, J. W., Yano, J. & Borovik, A. S. Assembly and properties of heterobimetallic $\text{Co}^{\text{III}}/\text{Ca}^{\text{II}}$ complexes with aquo and hydroxo ligands. *J. Am. Chem. Soc.* **134**, 17526–17535 (2012).
44. Rigby, M. L. *et al.* Cobalt analogs of Ru-based water oxidation catalysts: overcoming thermodynamic instability and kinetic lability to achieve electrocatalytic O_2 evolution. *Chem. Sci.* **3**, 3058–3062 (2012).
45. Rohde, J. U. *et al.* Crystallographic and spectroscopic characterization of a nonheme Fe(IV)=O complex. *Science* **299**, 1037–1039 (2003).
46. Xu, X. L., Chen, Z. H., Li, Y., Chen, W. K. & Li, J. Q. Bulk and surface properties of spinel Co_3O_4 by density functional calculations. *Surf. Sci.* **603**, 653–658 (2009).
47. Garcia Mota, M. *et al.* Importance of correlation in determining electrocatalytic oxygen evolution activity on cobalt oxides. *J. Phys. Chem. C* **116**, 21077–21082 (2012).
48. Chen, J. & Selloni, A. Water adsorption and oxidation at the $\text{Co}_3\text{O}_4(110)$ surface. *J. Phys. Chem. Lett.* **3**, 2808–2814 (2012).
49. Chivot, J., Mendoza, L., Mansour, C., Pauporte, T. & Cassir, M. New insight in the behaviour of $\text{Co-H}_2\text{O}$ system at 25–150 °C, based on revised Pourbaix diagrams. *Corros. Sci.* **50**, 62–69 (2008).
50. Yeo, B. S. & Bell, A. T. Enhanced activity of gold-supported cobalt oxide for the electrochemical evolution of oxygen. *J. Am. Chem. Soc.* **133**, 5587–5593 (2011).
51. Wang, L. P. & Van Voorhis, T. Direct-coupling O_2 bond forming a pathway in cobalt oxide water oxidation catalysts. *J. Phys. Chem. Lett.* **2**, 2200–2204 (2011).
52. Concepcion, J. J., Jurss, J. W., Templeton, J. L. & Meyer, T. J. Mediator-assisted water oxidation by the ruthenium ‘blue dimer’ *cis,cis*- $[(\text{bpy})_2(\text{H}_2\text{O})\text{RuORu}(\text{OH}_2)(\text{bpy})_2]^{4+}$. *Proc. Natl Acad. Sci. USA* **105**, 17632–17635 (2008).
53. Sivasankar, N., Weare, W. W. & Frei, H. Direct observation of a hydroperoxide surface intermediate upon visible light-driven water oxidation at an Ir oxide nanocluster catalyst by rapid-scan FT-IR spectroscopy. *J. Am. Chem. Soc.* **133**, 12976–12979 (2011).
54. Lever, A. B. P., Ozin, G. A. & Gray, H. B. Electron transfer in metal-dioxygen adducts. *Inorg. Chem.* **19**, 1823–1824 (1980).
55. Gamelin, D. R. Water splitting: Catalyst or spectator? *Nature Chem.* **4**, 965–967 (2012).
56. Agiral, A., Soo, H. S. & Frei, H. Visible light induced hole transport from sensitizer to Co_3O_4 water oxidation catalyst across nanoscale silica barrier with embedded molecular wires. *Chem. Mater.* **25**, 2264–2273 (2013).
57. Zhou, M., Robertson, G. P. & Roovers, J. Comparative study of ruthenium(II) tris(bipyridine) derivatives for electrochemiluminescence application. *Inorg. Chem.* **44**, 8317–8325 (2005).

Acknowledgements

This work was supported by the Director, Office of Science, Office of Basic Energy Sciences, Division of Chemical, Geological and Biosciences of the US Department of Energy (contract no. DE-AC02-05CH11231).

Author contributions

H.F. developed the set-up and designed the experiments. M.Z. and M.D.R. prepared the samples and conducted the rapid-scan FTIR experiments and electrochemical measurements. M.Z. performed the mass spectrometric measurements. H.F. and M.Z. wrote the paper.

Additional information

Supplementary information is available in the [online version](#) of the paper. Reprints and permissions information is available online at www.nature.com/reprints. Correspondence and requests for materials should be addressed to H.F.

Competing financial interests

The authors declare no competing financial interests.